Published in final edited form as:

ACS Nano. 2022 April 26; 16(4): 6813–6824. doi:10.1021/acsnano.2c01706.

Wavelength-Dependent Bifunctional Plasmonic Photocatalysis in Au/Chalcopyrite Hybrid Nanostructures

Xingda An[1,4], **Joshua C. Kays**[2,4], **Ian V. Lightcap**[5], **Tianhong Ouyang**[1,4], **Allison M. Dennis**[2,3,4], **Björn M. Reinhard**[1,4]

[1]Department of Chemistry, Boston University, Boston, MA 02215, USA.

[2]Department of Biomedical Engineering, Boston University, Boston, MA 02215, USA.

[3]Division of Materials Science and Engineering, Boston University, Boston, MA 02215, USA.

[4]The Photonics Center, Boston University, Boston, MA 02215, USA.

[5]Center for Sustainable Energy, University of Notre Dame, Notre Dame, IN 46556, USA.

Abstract

Excited, or “hot” charge carrier generation and transfer driven by the decay of localized surface plasmon resonances (LSPRs) are key steps in plasmonic photocatalysis. Hybrid structures that contain both metal and semiconductor building blocks facilitate the extraction of reactive charge carriers and their utilization for photoelectrocatalysis (PEC). Additional functionality arises from hybrid structures that combine noble metal nanostructures with semiconductor components, such as chalcopyrite ($CuFeS_2$) nanocrystals (NCs), which by themselves support quasistatic resonances. In this work, we use a hybrid membrane to integrate Au nanorods (NRs) with a longitudinal LSPR at 745 nm and $CuFeS_2$ NCs with a resonance peak at 490 nm into water-stable nanocomposites for robust and bifunctional photocatalysis of oxygen and hydrogen evolution reactions in a wavelength-dependent manner. Excitation of NRs or NCs in the nanocomposite correlates with increased hydrogen or oxygen evolution respectively, consistent with a light-driven electron transfer between the metal and semiconductor building blocks whose direction depends on the wavelength. The bifunctional photoreactivity of the nanocomposite is enhanced by Cu(I)/Cu(II)-assisted catalysis on the surface of the NCs.

Keywords

Plasmonic Photocatalysis; Hybrid Plasmonics; Chalcopyrite; Plasmonic Semiconductor Nanocrystals; Water Splitting

Corresponding Author: Björn M. Reinhard: bmr@bu.edu.

Author Contributions

B.M.R. and X.A. conceived the study and designed the experiments. X.A. performed the experiments assisted by T.O. and analyzed the data. J.C.K. synthesized and characterized the chalcopyrite nanocrystals. I.V.L performed the GC-TCD measurements. B.M.R and X.A wrote the manuscript with edits from J.C.K and A.M.D. All authors discussed the results and contributed to the manuscript.

Supporting Information.

The following files are available free of charge. Supporting Information (PDF) contains supplemental characterizations of the hybrid plasmonic photocatalyst L-NR-NCs and controls through SEM, TEM, EDX, photoelectrochemistry, UV-vis, XRD, XPS, Raman spectroscopy, and GC-TCD (Fig. S1–S2, Fig. S4–S15, Tables S1–S2); spectra for LED used in this work (Fig. S3); and supplemental experimental methods.

Introduction

Localized plasmons are coherent collective electron oscillations well known in noble metal nanoparticles (NPs)[1–3] and doped semiconductors.[4–6] The dipolar plasmon resonance wavelength is determined by the Fröhlich resonance condition $\varepsilon_1 = -2\varepsilon_m$, where ε_1 is the real part of the dielectric function of the plasmonic material and ε_m the dielectric constant of the ambient medium.[7] Intriguingly, it was shown that even pure semiconductors with strong interband transitions can also fulfill the Fröhlich resonance condition, an effect that has been referred to as "interband plasmonics".[8–9] Localized surface plasmon resonances (LSPR) in metals or semiconductors are of general interest as they can provide intense optical absorption and/or scattering cross-sections, and achieve strong local E-field localization. Furthermore, the non-radiative dissipation of plasmons can generate "hot" charge carriers and induce photothermal effects.[10–11] These fundamental properties form the basis of important applications of plasmonic NPs in chemical sensing,[12] high-contrast biomolecule or cell imaging,[13–14] photo-induced biomedical therapy,[10] and photocatalysis.[15–17]

Plasmonic photocatalysis utilizes plasmonic resonance effects for harvesting light, in particular sunlight, the most abundant energy source on earth, to facilitate chemical transformation and to convert sunlight into chemical energy.[15, 18–21] Plasmonic photocatalysis can occur through different mechanisms, of which i.) E-field enhancement of molecular or nanoscale photocatalysts[15, 18] or energy transfer through Plasmon-Induced Resonance Energy Transfers (PIRET),[22–23] and ii.) hot charge transfer-induced reactivity[19–20, 24] are the most widely studied. While the former utilizes plasmonic NPs as nanoantennas to generate a strong, resonant E-field-enhancement to boost the excitation of photocatalysts located in the immediate vicinity of the NPs, the latter involves charge transfer processes of the plasmonic component. Dephasing of plasmons is coupled to direct or indirect charge transfer mechanisms.[10] In direct transfer, charge carriers from the NP are directly transferred from their initial energy level to acceptor states of an associated molecule or semiconductor. In contrast, indirect transfer requires the generation of highly energetic, hot charge carriers in the metals in a first step that can subsequently transfer across the energetic barrier of the interface into acceptor states in a second step. Plasmonic hot charge carrier generation and injection into or emission from Au and Ag NPs have been characterized through *ab initio* calculations as well as ultrafast spectroscopy.[19, 25–27]

The occurrence and efficiency of plasmonic charge carrier transfers depend on various factors, including the size, composition and morphology of the NPs, the photoexcitation conditions, and the energetic alignment of excited charge carriers with acceptor levels in adsorbates.[28–29] These degrees of freedom provide opportunities for controlling plasmonic charge transfer processes in rationally designed plasmonic nanostructures and for driving redox processes. Charge separation mechanisms that increase the lifetimes of reactive charge carriers have been exploited in hybrid plasmonic structures comprising both noble metal NPs and semiconductor components to achieve clean energy conversion and photovoltaic cells,[16, 21, 30–31] to catalyze the synthesis of organic molecules,[32–33] for optoelectronic devices,[34] and for environmental remediation.[10, 35] Particularly, semiconductor nanocrystals, including oxides[25, 36–37] and other chalcogenides,[16, 38] perovskites,[39] and carbon-based

QDs,[40] among others,[26, 36, 41] have been utilized to assemble functional plasmonic hybrid materials. Interesting functionalities can be expected for semiconductor QDs that by themselves sustain quasistatic resonances. One aspect of control that is distinct to hybrid nanostructures comprising plasmonic metal and semiconductor components with distinct resonances is the ability to induce specific charge transfer processes through choice of the excitation wavelength. It is conceivable that the nature and direction of charge transfer in hybrid structures can be modulated through excitation of resonances associated with the different building blocks, which could make it feasible to prepare an excess of electrons or holes on the individual components for bifunctional catalysis of different reactions.

In this study, we investigate hybrid plasmonic photocatalysts comprising Au nanorods (NRs) encapsulated in a lipid membrane that contains chalcopyrite ($CuFeS_2$) nanocrystals (NCs). Importantly, the $CuFeS_2$ NCs sustain distinct quasistatic resonances when the Fröhlich resonance condition is met at around $\lambda_{res}^{NC} = 490$ nm,[8, 42–43] and the decay of this resonance results in hot electron production.[8, 44–45] They also offer favorable surface properties for adsorption of water and other oxygen species,[46] as well as a Cu(I)/Cu(II) couple that can contribute to redox catalysis. We evaluate the wavelength-dependent redox catalysis provided by the hybrid photocatalysts using hydrogen evolution (HER) and oxygen evolution reaction (OER) as test reactions. We demonstrate that the combination of Au NR and $CuFeS_2$ NCs into nanocomposites increases the photocatalytic activity of the building blocks, and that excitation of Au NR and $CuFeS_2$ resonances in the NIR and visible range of the electromagnetic spectrum is correlated with HER and OER catalysis, respectively. The observed wavelength-dependent catalysis is rationalized in a model in which light-driven electron-transfer and Cu(I)/Cu(II) redox couple-mediated catalysis on the surface of the NCs contribute to the overall catalytic effect.

Results and Discussion

Assembly and Characterization of Hybrid Plasmonic Photocatalysts

The lipid-nanorod-nanocrystal hybrid plasmonic photocatalyst (L-NR-NCs) was prepared *via* one-pot self-assembly and consists of a Au NR core (Fig. S1A) and chalcopyrite Cu(I)Fe(III)S_2 NCs integrated by a hybrid membrane formed by an inner octadecanethiol (ODT) layer tethered to the Au NR and outer lipid layer (Fig. 1A). The average width of the hybrid membrane in L-NR-NCs is 8.9 ± 2.7 nm as measured from TEM micrographs of the nanocomposites (Fig. 1B, see also Fig. S1B, C). The chalcopyrite NCs have an average diameter of 5.1 ± 0.4 nm (Fig. S1D) and a Fe:Cu ratio of 2.1:1 (Table S1). An approximate particle ratio of 125:1 (NCs:NR) is calculated from the measured Au and Cu concentrations. The membrane encapsulates the NCs and positions them in direct vicinity to the NR core as well as the membrane-solution interface (Fig. 1B). Energy Dispersive X-Ray Spectroscopy (EDX) element maps of L-NR-NCs also confirm the presence of Fe close to the Au NRs (Fig. S2A).

A series of characterization results corroborate successful L-NR-NCs formation. Correlated darkfield (DF) and fluorescence (FL) imaging of L-NR-NCs show strong spatial colocalization between the DF signal from the NR cores and the FL signal from a membrane

dye included in the lipid layer (Fig. S2B). Raman spectra of the purified nanocomposites contain characteristic peaks at 288 and 360 cm^{-1} (Fig. 1C), corresponding to the chalcopyrite A_1 and B_2 phonon modes, respectively.[47] Furthermore, X-Ray Diffraction (XRD) spectra for L-NR-NCs exhibit diffraction peaks at $2\theta = 29°$ and 49° (Fig. 1D), indicative of the chalcopyrite (112), and (220)/(204) peaks (Fig. 1E).[48] The XRD spectra also contain the Au NR (111), (200), (220) and (311) diffraction peaks at $2\theta = 38°$, 44°, 65° and 78°,[49] as well as the Si substrate signal at 52°.[50]

Consistent with previous reports,[8, 42] the chalcopyrite NCs sustain a strong quasistatic resonance at around $\lambda_{res}^{NC} = 490\,nm$ (Fig. 1F, inset; see also Fig. S1D). The Au NRs possess an intense longitudinal LSPR mode at around 745 nm as well as a vertical mode at around 520 nm, the latter of which overlaps with the NC resonance. A significant increase in absorption in the range of the high energy feature of the L-NR-NCs hybrid at around 510 nm (Fig. 1F) when compared to the separate NR and NC building blocks indicates a resonant plasmonic enhancement of the NC absorption through the vertical NR plasmon mode. The longitudinal NR mode at 745 nm allows for a resonant charge carrier excitation in the NR without overlap with the NC resonance.

Wavelength-Dependent Plasmonic Photocatalysis by L-NR-NCs

Chalcopyrite $CuFeS_2$ possesses an intermediate band (IB) formed by Fe 3d orbitals.[9] In the bulk, the gap between the valence band (VB) and IB has been reported as 0.63 eV;[8–9] whereas in chalcopyrite NCs, the band gap can be increased due to quantum confinement. For NCs of similar size and Cu/Fe ratios as used in this work, an optical band gap of approx. 1.4 eV was measured,[44, 51–52] which we assign to the VB-IB gap. The electron excited state energy has also been determined by Mott-Schottky plots to be −0.432 V (*vs.* NHE), which we assign to the IB position.[44] Collective electron-hole pair excitations from the VB into the IB give rise to the strong absorption resonance at λ_{res}^{NC}.[8] The VB-IB gap is indirect,[8] but in L-NR-NCs the vertical plasmon mode of the Au NR that energetically overlaps with the NC resonance can enhance the NC excitation in the near-field.

The presence of distinct NC- and NR-associated resonances in L-NR-NCs provides an experimental strategy for switching the redox potential of the NCs and for making it commensurable with either oxygen or hydrogen evolution reaction (OER/HER) (Fig. 2A, D). In particular, the dephasing of the NC resonance in L-NR-NCs can cause hot electron transfer from the NC to the Au NR through direct or indirect charge transfer pathways (Fig. 2A),[8, 44] resulting in charge separation and accumulation of holes on the NC surface, which can subsequently facilitate the oxygen evolution catalysis according to Eq. 1. Conversely, excitation of the longitudinal plasmon resonance of the Au NRs at around 745 nm is expected to facilitate electron transfer from the NR to the NC (Fig. 2D)[53–54] enabling the reduction of protons (Eq. 2).

$$4OH^- - 4e^- \rightarrow 2H_2O + O_2 \qquad \text{Eq. 1}$$

$$2H^+ + 2e^- \rightarrow H_2 \quad \text{Eq. 2}$$

To validate this model and test the efficiency of the photocatalyzed reactions, L-NR-NCs were drop-casted on a glassy carbon electrode for photoelectrochemical (PEC) characterizations. 1 M NaOH and 0.5 M H_2SO_4 were used as electrolyte for OER and HER, respectively, and the electrodes were irradiated with either a 530 nm LED (referred to as green light) or a 730 nm LED (referred to as red light) (see Fig. S3 for LED spectra). Control groups include lipid-wrapped Au NRs (L-NRs) (Fig. S2C), NCs, and a simple mixture of L-NR and NCs. All controls were prepared to contain the same NR and/or NC concentrations as L-NR-NCs.

Importantly, in 1 M NaOH, Linear Sweep Voltammetry (LSV) curves of L-NR-NCs show evident light responses that lead to enhanced photocurrent densities (J_{photo}) as well as earlier onset potentials around 0.3 V (*vs.* Ag/AgCl, same below unless otherwise stated) (Fig. 2B) compared to the dark curve or control groups under the same irradiation conditions (Fig. S4 and Table S2). In particular, although the simple mixture control contains identical components, L-NR-NCs achieve a higher catalytic performance due to the localization of NCs in close vicinity to the NRs. The vicinity effect not only enables an efficient plasmonic enhancement of NC excitation, but also facilitates electron transfer between the two components. The light response is further evidenced by photocurrent measurements from a short circuit current setup of L-NR-NCs with alternating light-on and -off cycles and 0 V applied bias (Fig. S5). The superior OER photocatalytic performance for L-NR-NCs with green-light irradiation is further evidenced by the lowest Tafel slope among all tested conditions (222 mV dec^{-1}, Fig. 2C), which is comparable to that of water splitting photoanodes in recent reports.[55]

A significant light-response is also recorded for L-NR-NCs-catalyzed HER under red-light irradiation in H_2SO_4. The early onset potential and high J_{photo} (Fig. 2E), as well as a low Tafel slope of 118 mV dec^{-1} (Fig. 2F) indicate a superior HER photocatalytic performance. A steady photocurrent of around 2 μA is observed within 1 hour of measurement with 15 on/off cycles (Fig. S5).

Chronoamperometry (CA) measurements in both electrolytes reveal that the L-NR-NCs maintain robust photocatalytic properties for over 6 hours of constant performance with a high J_{photo} compared to the dark curve or NCs only control (Fig. 2G). The stability of the L-NR-NCs performance is impressive, considering that chalcopyrite nanocrystals have been shown to dissolve quickly in acidic and neutral environments[44, 56] (see also Fig. S6). Quantification of the amount of Cu and Fe released into the aqueous medium from L-NR-NCs and NCs confirms that the integration into lipid-coated L-NR-NCs nanocomposites protects the NCs against dissolution in both acid and base electrolytes during a 6-hour CA measurement, as well as in water suspensions when stored up to 30 days (Fig. S6). The lipid membrane not only provides structural integrity to the hybrid material, but also increases the PEC stability of the membrane-encapsulated NCs.

LSV and CA curves of L-NR-NCs contain indications of an activation of the photo-catalysis in both acidic and basic electrolyte as a function of time under irradiation. This effect is particularly obvious when comparing the 1st and 100th scan with light in the LSV curves (Fig. 2B, F), and is attributed to Cu(I)/Cu(II) redox pair-mediated catalysis (see discussion below).

We probed the wavelength dependence (action spectrum) of the catalytic J_{photo} for L-NR-NCs in NaOH and H_2SO_4 in the 100th LSV cycle by measuring J_{photo} at 9 discrete wavelengths in the range between 395 – 730 nm. The action spectrum in the alkaline electrolyte show that the highest J_{photo} is achieved at 530 nm (Fig. 2H), corresponding to the high-energy absorbance band of the nanocomposite. Although the increase in J_{photo} with excitation closer to the UV suggests that interband absorption in the L-NR-NCs composite can also enhance OER photocatalysis, the distinct peak at 530 nm corroborates our hypothesis that excitation of the quasistatic NC resonance at λ_{res}^{NC} facilitates OER photocatalysis. The action spectrum recorded in H_2SO_4 reveals an increased J_{photo} at wavelengths that coincide with the longitudinal LSPR mode at around 745 nm (Fig. 2I). None of the individual components or the simple mixture control (Fig. S4, Fig. S8) achieved a comparable light response at these peak wavelengths.

Additional evidence of the wavelength-dependent enhancement of OER and HER catalysis is provided by the comparison of the PEC performances of L-NR-QDs with control nanocomposites prepared with identical NCs but containing Au or Ag nanosphere (NS) cores, referred to as L-Au-NCs or L-Ag-NCs. L-Au-NCs have an absorbance band at around 530 nm associated with the resonances in NCs and Au NSs (Fig. S7A). The LSPR of Ag NSs occurs at shorter wavelengths (420 nm) and has a weaker overlap with the NC resonance at λ_{res}^{NC}. Consequently, L-Ag-NCs show a weaker plasmonic enhancement of the NC absorption (Fig. S7B). In 1 M NaOH under green light irradiation, L-Au-NCs show a high J_{photo} as well as an early onset potential of OER around 0.3 V (*vs.* Ag/AgCl), comparable to L-NR-NCs and indicative of an enhanced catalysis under resonant excitation (Fig. S7C). In contrast, LSV curves of L-Ag-NCs controls show only a weak to moderate catalytic effect under either green light or 430 nm irradiation, which corroborates the hypothesis that the OER catalysis observed for L-NR-NCs derives from a plasmon-enhanced excitation of the NC resonance, and not from the metal core resonance. Notably, in acidic electrolyte, neither L-Au-NCs nor L-Ag-NCs achieved any evident HER photocatalysis under resonant excitation (Fig. S7D). This observation suggests that electron accumulation on NCs for HER is only efficient in hybrid structures, such as our L-NR-NCs, under excitation of a second plasmonic building block whose LSPR does not overlap with the NC resonance. The lack of a strong photocatalytic HER response at 530 nm for L-Au-NCs also provides experimental evidence that energy transfer from the metal plasmon to the NC, or plasmon-enhanced interband transitions in the NCs are not the driving factors for charge carrier formation and reactivity in case of the HER.

Another factor that contributes to the wavelength-dependent reactivity of the hybrid structure, in addition to intrinsic differences in photoreactivity between chalcopyrite NCs and metal NRs, is the structural design of L-NR-NCs. The metal NRs are shielded from

directly participating in chemical reactions at the nanocomposite-water interface by the lipid membrane layer. This shielding effect is detectable as difference between the onset potentials, light response and dark current densities of Au NR controls not coated with the hybrid membrane (Fig. S8) and L-NRs (Fig. S4A, B).

Plasmonic photothermal (PPT) heating is a factor that can potentially also contribute to the photocatalytic performance of LC-NR-NCs. However, given the relatively low power density of the illumination used (9.46 W/m^2), calculations of the temperature increase in the vicinity of Au NRs and chalcopyrite NCs (see SI)[43, 57] predict only a modest temperature increase ($\Delta T < 2.4$ K) under our continuous wave irradiation. An increase in the global temperature of around 2 °C was experimentally measured on the electrode surface during a 6-hour CA measurement of L-NR-NCs in either NaOH or H_2SO_4 (Fig. S9A). A change in temperature on the electrode surface of this magnitude had a negligible effect on the measured current density (Fig. S9B). Furthermore, the poor catalytic response measured from L-NRs, NCs, and the simple mixture control of L-NRs and NCs under irradiation (Fig. S4), as well as the distinct wavelength dependence of OER and HER for L-NR-NCs (Fig. 2H, I) also indicate that photothermal heating is not the main cause for the observed increase in OER and HER.

Role of the Cu(I)/Cu(II) Redox Couple in Plasmonic Photocatalysis by L-NR-NC

Intriguingly, the shapes of the LSV curves for OER and HER with L-NR-NCs change as the cycling continues in NaOH or H_2SO_4. The 1st LSV scans under light irradiation contain a distinct oxidation peak onset around 0.8 V (*vs.* Ag/AgCl) in NaOH (Fig. 2B, solid curve), and a reduction peak at −0.3 V in H_2SO_4 (Fig. 2E, solid curve). Based on their redox potentials and *in situ* Raman characterizations (see below), these two peaks are assigned to the oxidation of the Cu(I) species in the NCs to Cu(II), and the reduction of Cu(II) to Cu(I).[58–59] In the 100th LSV scan under light irradiation, these peaks are no longer detected, but the overall current densities are significantly higher than in the 1st cycle for both OER and HER. From the 100th LSV scan of L-NR-NCs in NaOH (Fig. 2B), a maximum applied bias photon-to-current efficiency (ABPE) of 2.1% is calculated at 1.04 V *vs.* RHE (see SI for calculations), which is comparable to what was observed with previously described photoanodes.[60] The increase in current density is also observed in CA curves in H_2SO_4 or in NaOH within the first 30 min of measurements (Fig. 2G), which indicates a self-accelerating photocatalytic process for both half reactions. In NaOH, the increase in current density is transient and diminishes at later time points (Fig. 2G, top), whereas in H_2SO_4 the current density increases throughout the duration of the CA experiment (Fig. 2G, bottom).

We attribute the increase in OER and HER J_{photo} to an augmentation of the plasmonic charge transfer mediated catalysis by a Cu(I)/Cu(II) redox pair-coupled catalysis (Fig. 3A). During the LSV scans in the alkaline electrolyte, LSPR excitation can induce electron transfer from NCs to NRs. Excess electrons associated with the Au NRs subsequently transfer to the electrode under the positive applied bias, generating the anodal photocurrent. The holes remaining on the NCs in this process are neutralized through two complementing mechanisms: i.) direct plasmonic photocatalysis of water oxidation (Fig. 3A, process (1)), and ii.) oxidation of Cu(I) into Cu(II) oxide (process (2)).[61] Metal oxides have favorable binding energies for OH^- and other reaction intermediates,[62] which is generally beneficial

for increasing the OER efficiency. Importantly, the Cu(II) species generated according to the second mechanism can also participate in water oxidation under regeneration of Cu(I). Both OER catalytic pathways can be summarized in Eq. 3, where "x" denotes the relative contribution of the Cu(I)-mediated catalytic mechanism.[63] Excessive Cu(I) oxidation in the process of hole neutralization is, however, expected to deteriorate the optical properties and surface conductivity of the NCs (Fig. S10). This effect can account for the observation that the increase in current density in the OER diminishes after approx. 30 min as the scanning continues (Fig. 2G, top).

According to the model in Fig. 3A, excitation of the longitudinal NRs LSPR in L-NR-NCs in H_2SO_4 results in an electron transfer from Au NR to NCs and yields an accumulation of excited electrons at the NC surface. Electron deficits on the NRs are balanced by the electrode. The excess electrons on the NCs are available not only for driving the direct HER plasmonic photocatalysis (Fig. 3A, process (3)), but also for reducing any surface-available Cu(II) back to Cu(I) (process (4)). Cu(I) has a standard oxidation potential of −0.15 V (*vs.* NHE), and is likely to facilitate the proton reduction reaction (0 V *vs.* NHE) while being oxidized to Cu(II) (Eq. 4), as has been shown in some previous reports.[64] The negative applied bias during HER can drive the reduction of the generated Cu(II) back to the predominant Cu(I) oxidation state in the NCs, preventing an excessive NC oxidation. As a result, different from the OER, the HER shows a steady increase in current density with increasing time (Fig. 2G, bottom).

$$xCu^{2+} + 4OH^- - (4 - x)e^- \rightarrow O_2 + xCu^+ + 2H_2O \quad \text{Eq. 3}$$

$$xCu^+ + 2H^+ + (2 - x)e^- \rightarrow xCu^{2+} + H_2 \quad \text{Eq. 4}$$

XRD and X-Ray Photoelectron Spectroscopy (XPS) measurements of L-NR-NCs and NCs confirm the outlined changes in the Cu oxidation states. In the XRD spectra of drop-casted L-NR-NCs thin films scanned in either 1 M NaOH or 0.5 M H_2SO_4 for 1 hour in the same conditions as used in the PEC measurements (Fig. 3B), signature diffraction peaks for NCs at $2\theta = 29°$ and 49°, and for NRs at 38°, 44°, 65°, 78° as discussed above are still observed. These signals confirm that the L-NR-NCs nanocomposites are structurally intact. Importantly, a distinct peak at $2\theta = 39°$ appeared after scanning in base (Fig. 3B, bottom), which is consistent with the (111) peak of CuO.[65] XRD spectra of L-NR-NCs recorded at different scanning times in NaOH reveal that the intensity of the CuO peak grows over time (Fig. S11A). The intensity of this peak is very low before treatment and is absent in the spectrum after scanning in H_2SO_4, suggesting that scanning in acid partially removes surface oxides. This surface oxidation of Cu in NCs also led to a redshift of the high-energy absorption band of the nanocomposite as well as a decrease in intensity in the UV-vis absorption spectra (Fig. S10). A similar trend is observed in XPS measurements. The Cu $2p_{3/2}$ XPS spectra of the NCs before any treatment contain a predominant Cu(I) peak at around 932.0 eV with a fitted peak area accounting for 87.1% of the entire signal (Fig. 3C).[66] A modest Cu(II) contribution (12.9%) at 934.1 eV indicates that some oxidation occurred during the preparation of the NCs. Notably, the Cu(II) percentage shows

a significant increase after the NCs have been scanned in 1 M NaOH (933.9 eV, 30.9%; Fig. 3D). A similar increase is also observed in the oxygen 1s spectra. The integrated signal that corresponds to metal oxides[67] at ~530 eV increases from 10.7% (Fig. 3E) to 21.3% after scanning in NaOH (Fig. 3F). In contrast, cycling of NCs in 0.5 M H_2SO_4 reduces the contributions from both Cu(II) (933.8 eV, 11.6%; Fig. S11B) and oxides (529.3 eV, 10.1%; Fig. S11C) compared to before treatment (Fig. 3C, E), revealing that the oxides were partially reduced. The Fe XPS spectra of the NCs or Au spectra of L-NR-NCs recorded before and after cycling show no significant differences (Fig. S12) and indicate that the Au NRs are shielded from participating in the redox catalysis and that Fe redox pairs do not significantly contribute to the catalytic mechanism. Overall, the XRD and XPS results support the hypothesis that Cu(I)/Cu(II) redox pair-coupled catalysis accompanies and enhances the direct plasmonic charge transfer-induced photoreactivity.

The plasmonic charge transfer and Cu-mediated catalytic mechanisms was further evidenced by Raman spectroscopy. We first probed the Raman spectra of the hybrid plasmonic photocatalyst at different excitation wavelengths on or off resonance (Fig. 4A). For all wavelengths, the A_1 and B_2 chalcopyrite phonon modes are still observed at around 290 and 350 cm^{-1}, respectively. Importantly, under near-resonant excitation (532 nm) of the high-energy feature of the nanocomposites, a broad band is observed in the Raman spectrum between 400 and 500 cm^{-1}, which is not present if the samples are excited off-resonance. This feature can be attributed to the presence of various oxygen species of Cu, such as oxides, hydroxides or hydroxyl radicals.[68–70] Although similar features are observed for NCs only, and a simple mixture control of Au NRs and NCs (Fig. S13), they are much less evident for these systems than for the nanocomposites.

For the nanocomposites, we monitored the intensity of the 400 – 500 cm^{-1} band at an excitation wavelength of 532 nm with different applied bias to probe for signatures of potential reaction intermediates (Fig. 4B). With an applied bias at or above 0.8 V (*vs.* RHE), the intensity of the Cu hydroxide band begins to increase. At an even higher voltage input of 1.4 V, the band further broadens and extends beyond 500 cm^{-1}. This broadening is consistent with hydroxyl intermediate formation on Au as previously reported[24] and was also experimentally validated with Au NR controls (Fig. S13A, D). However, this feature was not present at voltage input ranges corresponding to our PEC measurements (0 – 1.2 V). In addition, our Raman studies also do not indicate the presence of Fe-oxygen intermediates of water oxidation, which are typically found between 600 – 700 cm^{-1}.[71] Although, considering the redox potentials and the abundance of Fe in the NCs, it is conceivable that Fe(III) is reduced and contributes to the redox catalysis, our XRD, XPS, and Raman measurements do not support a significant contribution from the Fe-mediated redox cycles and, instead, point towards the Cu(I)/Cu(II)-mediated catalytic mechanism.

Overall, the SERS data are consistent with the formation of reactive holes in the NCs of the hybrid plasmonic photocatalyst upon excitation of the quasistatic collective NC resonance that results in a Cu-mediated redox process in the OER catalysis.

Photoelectrocatalysis with Sacrificial Reductant

To further illuminate the role of the Cu(I)/Cu(II) redox pair in the OER plasmonic photocatalysis of L-NR-NCs, we added Na_2SO_3 as a commonly used sacrificial reductant (SR) for OER photocatalysts into the alkaline electrolyte during PEC analysis.[60, 72] The SR reduces generated Cu(II) back to Cu(I) and, thus, prevents an accumulation of oxides on the NC surface (Fig. S14A). In the LSV curves of L-NR-NCs in 1 M NaOH and 0.5 M SR, the current densities of the 1st and 100th scans under excitation of the NCs LSPR show a similar activation behavior as discussed above without the SR (Fig. 5A). In the 100th LSV scan, a very early onset potential < 0.2 V (*vs.* Ag/AgCl, Table S2) as well as a high current density that peaks at over 160 mA cm^{-2} at around 0.7 V is detected. The Cu(I) oxidation at around 0.8 V is evidently broadened in the presence of SR due to the redox-coupling with the sulfite oxidation in the SR at 0.5 V (Fig. 5A, see also Fig. S14B). This redox-coupling is further corroborated by the observation that the J_{photo} recorded here in 1 M NaOH + 0.5 M SR is much higher than the cumulative J_{photo} for 1 M NaOH (Fig. 2B) and 0.5 M SR (Fig. S14C). The Tafel slope of L-NR-NCs irradiated in the green is 69 mV dec^{-1}, lower than for all control groups under identical illumination conditions (Fig. 5B).

The photocatalysis in the presence of the SR (Fig. 5C) shows an identical wavelength dependence as observed in NaOH. However, in the presence of the SR, the increase in current density in the CA curve is no longer a transient effect. Instead, a continuous increase for the entire duration of the experiment is observed (Fig. 5D). This change is attributed to a rapid reduction of Cu(II) to Cu(I) caused by the SR. Consequently, the current density is no longer limited by the depletion of surface accessible Cu(I). This model is supported by the LSV curve of L-NR-NCs performed in the presence of SR after the 6-hour CA measurement, which still contains a Cu(I) oxidation peak at 0.8 V (Fig. S14B). The rapid replenishment of Cu(I) sustains a continuous Cu(I)/Cu(II) catalytic cycle on the NC surface while maintaining the enhanced photocatalysis through excitation of the chalcopyrite NC resonance. Combined, these two factors account for the sustained increase in current density.

In the presence of the SR, the charge separation efficiency (η_{sep}) of the hybrid plasmonic photocatalyst can be calculated from the LSV curves and Eq. 5:[72]

$$\eta_{sep} = \frac{J_{photo}}{J_{abs} \times \eta_{inj}} \quad \text{Eq. 5}$$

where J_{photo} is the measured photocurrent density; J_{abs} is the theoretical current density (799 mA/cm^2, see SI) and is determined by the absorbed light power; and η_{inj} is the charge injection efficiency. The η_{inj} for Au-based systems have been previous reported to be 10 – 40% for Au-based particulate photocatalysts.[73–74] However, for consistency and comparison purpose with previous reports,[72] η_{inj} was assumed to be 100% in the presence of SR, which yields a maximum η_{sep} of 21.2% at 0.68 V from the LSV curve after activation (Fig. 5A). This value is comparable to that of state-of-the-art semiconductor array photoanodes.[72]

H_2 and O_2 production from the photocatalytic system was evidenced by gas chromatography with a thermal conductivity detector (GC-TCD) under 1-sun illumination (100 mW cm^{-2}) and with a three electrode setup where the L-NR-NCs nanocomposites-coated ITO

electrodes served as both the photoanode and cathode, and 0.5 M Na_2SO_3 was used as electrolyte (Fig. S15). After 2 hours of scanning with a 0.6 V (*vs.* Ag/AgCl) applied bias, 9.1 nmol H_2 was detected in 1 mL sampled air, which led to an overall water splitting Faradaic Efficiency of 15.5% (see SI).

Conclusions

In summary, we have demonstrated that the hybrid plasmonic photocatalyst L-NR-NCs, which contains chalcopyrite nanocrystals embedded in a protective lipid layer around a Au nanorod, achieves bifunctional photocatalysis as demonstrated for HER and OER through light-induced, wavelength-dependent photoreactivity. The self-assembled lipid membrane effectively prevents the dissolution of the chalcopyrite NCs and provides important PEC stability to the hybrid photocatalyst. The wavelength dependence of the photoelectrocatalysis in the presence of L-NR-NCs in alkaline electrolyte supports a model in which the near-field enhanced excitation of the NCs at $\lambda_{res}^{NC} = 490$ nm results in electron transfer from the NCs to the NR under the formation of holes on the NCs for an efficient catalysis of the OER. Conversely, excitation of the Au NR longitudinal plasmon resonance at 745 nm drives electron transfer from the NR to the NCs for HER photocatalysis in acidic electrolyte. The charge transfer-induced photocatalysis on the NCs is complemented by a Cu(I)/Cu(II) redox pair-mediated catalysis that provides a further enhancement of the catalytic performance of the OER and HER test reactions.

This work broadens the applicability of semiconductor nanocrystals in plasmonic charge carrier-mediated photocatalysis and introduces a general framework for modulating charge transfer through nanoassemblies containing multiple components with discrete quasistatic resonances at different wavelengths for multifunctional photocatalysis. L-NR-NCs achieve a high ABPE of 2.1% in alkaline electrolyte, and a charge separation efficiency of 21.2% in the presence of a sacrificial reductant. These competitive performance metrics[60, 72] underline the potential of the L-NR-NCs platform for enhancing the efficiency of sustainable light energy harvesting.

Experimental

Synthesis of Au NRs.

Au nanorods (NRs) were synthesized through a modified seed-mediated growth approach as previously reported.[75] Seed solution was prepared by first mixing water solutions of cetyltrimethylammonium bromide (CTAB, 0.37g, 10 mL; Sigma Aldrich) and $HAuCl_4$ (2 mg, 0.2 mL; Sigma Aldrich), and then fast injection of 480 μL of a reducing agent containing 10 mM $NaBH_4$ and 10 mM NaOH with rapid stirring. The color of the seed solution turned dark brown after adding the reducing agent. For NR growth, a growth mixture containing water solutions of CTAB (3.7 g, 100 mL) and $HAuCl_4$ (20 mg, 2 mL) was prepared. Into this mixture was added 80 μL 0.1 M $AgNO_3$ and 5 mL 0.1 M hydroquinone (both from Sigma Aldrich) water solutions. Finally, 1.6 mL seed solution was added into the growth mixture with fast stirring, and the mixture was allowed to grow overnight before being centrifuged, washed three times with DI water, and stored at 4 °C for

further use. An average length of 122.9 ± 12.9 nm and width of 46.9 ± 5.9 nm (aspect ratio of 2.62) are calculated based on electron microscopy images of 50 NRs.

Preparation of the Hybrid Plasmonic Photocatalyst.

L-NR-NCs were synthesized in a modified one-pot self-assembly approach.[14–15] First, Chloroform solutions of 55 mol% DPPC, 5 mol% DOPS, and 40 mol% cholesterol (all from Avanti Polar Lipids) were mixed with a 40 μL of NCs chloroform suspension, whose concentration is shown in Table S1. A total lipid amount of 2 μmol was used. The mixture was rotary evaporated at 32 °C to remove the solvent, desiccated overnight, and resuspended into liposome water suspensions through tip sonication. Afterwards, 80 μL 2 mg/mL octadecanethiol (ODT, Sigma Aldrich) ethanol solution and 1 mL 10^{10} particle/mL Au NRs colloid were added into the liposome suspension. The mixture was shaken in dark at RT for 12 hours before being centrifuged, washed with water, combined and stored at 4 °C for later use.

Raman Characterization of the Hybrid Plasmonic Photocatalyst.

Raman measurements in Fig. 1C were performed on drop-casted thin films of L-NR-NCs and controls on Si wafer substrates (<100>, University Wafers) with a Renishaw InVia Raman Microscope with a 100x air objective (Leica, Numerical Aperture=0.85), 2400 l/mm diffraction grating, 532 nm excitation laser, 60-seconds exposure time, and laser powers of 1.6×10^3 μW. Each spectrum was calibrated with the Si peak at 522 cm^{-1}, and Lorentzian peak fitting of Raman spectra was performed in Origin for calculation of peak positions, peak FWHMs as well as the integrated peak areas. At least 10 spectra were collected under each condition for statistical analyses. For Raman measurements in Fig. 4, samples were drop-casted on ITO substrates and measured on the Renishaw Raman Microscope. 532 nm, 633 nm and 785 nm excitation laser were used with comparable laser powers around 1.6×10^3 μW. Applied bias was administered with an Olympus power supplier.

Structural Characterization of the Hybrid Plasmonic Photocatalyst.

For the correlated DF/FL imaging of L-NR-NCs with a membrane dye to test successful lipid wrapping (Fig. S2B), 3 mol% DSPE-PEG(2000)-Biotin (1,2-distearoyl-sn-glycero-3-phosphoethanolamine-N-[biotinyl(polyethylene glycol)-2000](ammonium salt), Avanti Polar Lipids) was included in the preparation, and the DPPC was reduced to 52 mol% to keep the total lipid amount constant. The remaining synthesis procedures are identical to described above. 17 μL 1 mg/mL solution of a streptavidin Alexa Fluor 594 (ThermoFisher) dye in 0.5x Phosphate Buffered Saline (PBS) was then added to 50 μL of the nanocomposite suspension and incubated in dark at RT for 2 hours. After centrifuging and washing twice with 0.5x PBS buffer, the samples were observed under an Olympus IX71 Inverted Microscope for DF and FL imaging with an Olympus 60x oil objective (NA = 0.65–1.25). Images were analyzed by ImageJ, and Manders coefficients were calculated with the JACoP ImageJ plugin.[76] X-Ray Diffraction spectra were acquired on a Bruker D2 Phaser XRD with a 2 mm receiving slit and a 2.5° Söller slit.

Photoelectrochemical Measurements.

Linear Sweep Voltammetry (LSV) and Chronoamperometry (CA) curves were measured on a Gamry Instruments potentiostat in a three-electrode setup with a 3 mm-diameter glassy carbon working electrode, a standard Ag/AgCl reference electrode and a platinum wire counter electrode (all purchased from BASI Analytical Instruments). LSV curves were collected in 1 M NaOH, 0.5 M H_2SO_4, 1 M NaOH + 0.5 M Na_2SO_3 as a sacrificial reductant (SR), or 0.5 M SR only for control. A scan rate of 50 mV/s and a collection rate of 10 Hz was used in LSV measurement; an applied bias of 800 mV (vs Ag/AgCl, same below unless otherwise stated) for alkaline electrolytes or −700 mV in acidic electrolyte, and a collection rate of 1 Hz were used in the CA measurement. For illumination, collimated LEDs (Thorlabs) were used. Green-light illumination was with an LED with nominal wavelength of 530 nm and a measured power density of 9.46 μW mm^{-2} was used; and red-light illumination was with a 730 nm LED, the power density was controlled to be the same by an LED driver. For the wavelength-dependence tests (action spectra measurements, Fig. 2H, I and Fig. 5C), LEDs with nominal wavelengths at 395, 420, 430, 450, 460, 530, 565, 620, 730 nm were used, all were controlled to have the same power.

Supplementary Material

Refer to Web version on PubMed Central for supplementary material.

ACKNOWLEDGMENT

The authors thank the MSE core facilities at Boston University for the use of XRD diffractometer, and Dr. Greg Lin for XPS measurements. This work was performed in part at the Center for Nanoscale Systems (CNS), a member of the National Nanotechnology Coordinated Infrastructure Network (NNCI), which is supported by the National Science Foundation under NSF award no. 1541959. CNS is part of Harvard University.

Funding Sources

B.M.R. acknowledges support from the National Institutes of Health (R01CA138509, R01GM142012) and the National Science Foundation (CHE-1808241). A.M.D. acknowledges support from the National Institutes of Health (R21GM135849), and J.C.K. acknowledges support through a National Science Foundation Graduate Research Fellowship (NSF-GRFP; DGE-1840990).

REFERENCES

1. Amendola V; Pilot R; Frasconi M; Maragò OM; Iatì MA, Surface plasmon resonance in gold nanoparticles: a review. Journal of Physics: Condensed Matter 2017, 29 (20), 203002.
2. Hong Y; Reinhard BM, Optoplasmonics: basic principles and applications. Journal of Optics 2019, 21 (11), 113001.
3. Halas NJ; Lal S; Chang W-S; Link S; Nordlander P, Plasmons in strongly coupled metallic nanostructures. Chemical reviews 2011, 111 (6), 3913–3961. [PubMed: 21542636]
4. Agrawal A; Cho SH; Zandi O; Ghosh S; Johns RW; Milliron DJ, Localized surface plasmon resonance in semiconductor nanocrystals. Chemical reviews 2018, 118 (6), 3121–3207. [PubMed: 29400955]
5. Xi M; Reinhard B r. M., Localized surface plasmon coupling between mid-IR-resonant ITO nanocrystals. The Journal of Physical Chemistry C 2018, 122 (10), 5698–5704.
6. Luther JM; Jain PK; Ewers T; Alivisatos AP, Localized surface plasmon resonances arising from free carriers in doped quantum dots. Nature materials 2011, 10 (5), 361–366. [PubMed: 21478881]
7. Maier SA, Plasmonics: fundamentals and applications, Springer-Verlag US: New York, NY, 2007.

8. Gaspari R; Della Valle G; Ghosh S; Kriegel I; Scotognella F; Cavalli A; Manna L, Quasi-static resonances in the visible spectrum from all-dielectric intermediate band semiconductor nanocrystals. Nano letters 2017, 17 (12), 7691–7695. [PubMed: 29125777]
9. Oguchi T; Sato K; Teranishi T, Optical reflectivity spectrum of a CuFeS2 single crystal. Journal of the Physical Society of Japan 1980, 48 (1), 123–128.
10. An X; Erramilli S; Reinhard BM, Plasmonic nano-antimicrobials: properties, mechanisms and applications in microbe inactivation and sensing. Nanoscale 2021, 13 (6), 3374–3411. [PubMed: 33538743]
11. Zhan C; Liu B-W; Huang Y-F; Hu S; Ren B; Moskovits M; Tian Z-Q, Disentangling charge carrier from photothermal effects in plasmonic metal nanostructures. Nature communications 2019, 10 (1), 1–8.
12. Mayer KM; Hafner JH, Localized surface plasmon resonance sensors. Chemical reviews 2011, 111 (6), 3828–3857. [PubMed: 21648956]
13. Zhang S; Reinhard B. r. M., Characterizing large-scale receptor clustering on the single cell level: a comparative plasmon coupling and fluorescence superresolution microscopy study. The Journal of Physical Chemistry B 2019, 123 (26), 5494–5505. [PubMed: 31244098]
14. An X; Majumder A; McNeely J; Yang J; Puri T; He Z; Liang T; Snyder JK; Straub JE; Reinhard BM, Interfacial hydration determines orientational and functional dimorphism of sterol-derived Raman tags in lipid-coated nanoparticles. Proceedings of the National Academy of Sciences 2021, 118 (33) e2105913118.
15. An X; Stelter D; Keyes T; Reinhard BM, Plasmonic photocatalysis of urea oxidation and visible-light fuel cells. Chem 2019, 5 (8), 2228–2242.
16. Li J; Cushing SK; Zheng P; Senty T; Meng F; Bristow AD; Manivannan A; Wu N, Solar hydrogen generation by a CdS-Au-TiO2 sandwich nanorod array enhanced with Au nanoparticle as electron relay and plasmonic photosensitizer. Journal of the American Chemical Society 2014, 136 (23), 8438–8449. [PubMed: 24836347]
17. Wilson AJ; Mohan V; Jain PK, Mechanistic understanding of plasmon-enhanced electrochemistry. The Journal of Physical Chemistry C 2019, 123 (48), 29360–29369.
18. Linic S; Christopher P; Ingram DB, Plasmonic-metal nanostructures for efficient conversion of solar to chemical energy. Nature materials 2011, 10 (12), 911–921. [PubMed: 22109608]
19. Linic S; Chavez S; Elias R, Flow and extraction of energy and charge carriers in hybrid plasmonic nanostructures. Nature Materials 2021, 1–9. [PubMed: 33340007]
20. Zhang Y; He S; Guo W; Hu Y; Huang J; Mulcahy JR; Wei WD, Surface-plasmon-driven hot electron photochemistry. Chemical reviews 2017, 118 (6), 2927–2954. [PubMed: 29190069]
21. Wilson AJ; Jain PK, Light-Induced Voltages in Catalysis by Plasmonic Nanostructures. Accounts of chemical research 2020, 53 (9), 1773–1781. [PubMed: 32786334]
22. Li J; Cushing SK; Meng F; Senty TR; Bristow AD; Wu N, Plasmon-induced resonance energy transfer for solar energy conversion. Nature Photonics 2015, 9 (9), 601–607.
23. Li J; Cushing SK; Zheng P; Meng F; Chu D; Wu N, Plasmon-induced photonic and energy-transfer enhancement of solar water splitting by a hematite nanorod array. Nature communications 2013, 4 (1), 1–8.
24. Graf M; Vonbun-Feldbauer GB; Koper MT, Direct and Broadband Plasmonic Charge Transfer to Enhance Water Oxidation on a Gold Electrode. ACS nano 2021, 15 (2), 3188–3200. [PubMed: 33496564]
25. Van Turnhout L; Hattori Y; Meng J; Zheng K; Sá J, Direct Observation of a Plasmon-Induced Hot Electron Flow in a Multimetallic Nanostructure. Nano letters 2020, 20 (11), 8220–8228. [PubMed: 33095592]
26. Tagliabue G; DuChene JS; Abdellah M; Habib A; Gosztola DJ; Hattori Y; Cheng W-H; Zheng K; Canton SE; Sundararaman R, Ultrafast hot-hole injection modifies hot-electron dynamics in Au/p-GaN heterostructures. Nature Materials 2020, 19 (12), 1312–1318. [PubMed: 32719510]
27. Tan S; Argondizzo A; Ren J; Liu L; Zhao J; Petek H, Plasmonic coupling at a metal/semiconductor interface. Nature Photonics 2017, 11 (12), 806–812.
28. Manjavacas A; Liu JG; Kulkarni V; Nordlander P, Plasmon-induced hot carriers in metallic nanoparticles. ACS nano 2014, 8 (8), 7630–7638. [PubMed: 24960573]

29. Besteiro LV; Kong X-T; Wang Z; Hartland G; Govorov AO, Understanding hot-electron generation and plasmon relaxation in metal nanocrystals: Quantum and classical mechanisms. Acs Photonics 2017, 4 (11), 2759–2781.
30. Tanaka A; Teramura K; Hosokawa S; Kominami H; Tanaka T, Visible light-induced water splitting in an aqueous suspension of a plasmonic Au/TiO 2 photocatalyst with metal co-catalysts. Chemical science 2017, 8 (4), 2574–2580. [PubMed: 28553490]
31. Mubeen S; Lee J; Singh N; Krämer S; Stucky GD; Moskovits M, An autonomous photosynthetic device in which all charge carriers derive from surface plasmons. Nature nanotechnology 2013, 8 (4), 247–251.
32. Guo X; Hao C; Jin G; Zhu HY; Guo XY, Copper nanoparticles on graphene support: an efficient photocatalyst for coupling of nitroaromatics in visible light. Angewandte Chemie International Edition 2014, 53 (7), 1973–1977. [PubMed: 24505013]
33. Robatjazi H; Bao JL; Zhang M; Zhou L; Christopher P; Carter EA; Nordlander P; Halas NJ, Plasmon-driven carbon–fluorine (C (sp 3)–F) bond activation with mechanistic insights into hot-carrier-mediated pathways. Nature Catalysis 2020, 3 (7), 564–573.
34. Huang X; Li H; Zhang C; Tan S; Chen Z; Chen L; Lu Z; Wang X; Xiao M, Efficient plasmon-hot electron conversion in Ag–CsPbBr 3 hybrid nanocrystals. Nature communications 2019, 10 (1), 1–8.
35. Xu S; Guo L; Sun Q; Wang ZL, Piezotronic effect enhanced plasmonic photocatalysis by AuNPs/BaTiO3 heterostructures. Advanced Functional Materials 2019, 29 (13), 1808737.
36. Sadeghi SM; Gutha RR; Wing WJ, Impact of the Plasmonic Metal Oxide-Induced Photocatalytic Processes on the Interaction of Quantum Dots with Metallic Nanoparticles. The Journal of Physical Chemistry C 2020, 124 (7), 4261–4269.
37. Hattori Y; Meng J; Zheng K; Meier de Andrade A; Kullgren J; Broqvist P; Nordlander P; Sá J, Phonon-Assisted Hot Carrier Generation in Plasmonic Semiconductor Systems. Nano letters 2021, 21 (2), 1083–1089. [PubMed: 33416331]
38. Kawawaki T; Wang H; Kubo T; Saito K; Nakazaki J; Segawa H; Tatsuma T, Efficiency enhancement of PbS quantum dot/ZnO nanowire bulk-heterojunction solar cells by plasmonic silver nanocubes. ACS nano 2015, 9 (4), 4165–4172. [PubMed: 25785476]
39. Shi Z; Li Y; Li S; Li X; Wu D; Xu T; Tian Y; Chen Y; Zhang Y; Zhang B, Localized surface plasmon enhanced all-inorganic perovskite quantum dot light-emitting diodes based on coaxial core/shell heterojunction architecture. Advanced Functional Materials 2018, 28 (20), 1707031.
40. Yeh TF; Teng CY; Chen SJ; Teng H, Nitrogen-doped graphene oxide quantum dots as photocatalysts for overall water-splitting under visible light Illumination. Advanced materials 2014, 26 (20), 3297–3303. [PubMed: 24677453]
41. Cai X; Mao L; Yang S; Han K; Zhang J, Ultrafast charge separation for full solar spectrum-activated photocatalytic H2 generation in a black phosphorus–Au–CdS heterostructure. ACS Energy Letters 2018, 3 (4), 932–939.
42. Sugathan A; Bhattacharyya B; Kishore V; Kumar A; Rajasekar GP; Sarma D; Pandey A, Why does CuFeS2 resemble gold? The journal of physical chemistry letters 2018, 9 (4), 696–701. [PubMed: 29343063]
43. Ghosh S; Avellini T; Petrelli A; Kriegel I; Gaspari R; Almeida G; Bertoni G; Cavalli A; Scotognella F; Pellegrino T, Colloidal CuFeS2 nanocrystals: Intermediate Fe d-band leads to high photothermal conversion efficiency. Chemistry of Materials 2016, 28 (13), 4848–4858. [PubMed: 29033496]
44. Ge Q; Feng X; Wang R; Zheng R; Luo S; Duan L; Ji Y; Lin J; Chen H, Mixed Redox-Couple-Involved Chalcopyrite Phase CuFeS2 Quantum Dots for Highly Efficient Cr (VI) Removal. Environmental science & technology 2020, 54 (13), 8022–8031. [PubMed: 32412745]
45. Sandroni M; Wegner KD; Aldakov D; Reiss P, Prospects of chalcopyrite-type nanocrystals for energy applications. ACS Energy Letters 2017, 2 (5), 1076–1088.
46. Wei Z; Li Y; Gao H; Zhu Y; Qian G; Yao J, New insights into the surface relaxation and oxidation of chalcopyrite exposed to O2 and H2O: A first-principles DFT study. Applied Surface Science 2019, 492, 89–98.

47. Kumar P; Uma S; Nagarajan R, Precursor driven one pot synthesis of wurtzite and chalcopyrite CuFeS 2. Chemical Communications 2013, 49 (66), 7316–7318. [PubMed: 23852420]
48. Xie H; Su X; Zheng G; Zhu T; Yin K; Yan Y; Uher C; Kanatzidis MG; Tang X, The role of Zn in chalcopyrite CuFeS2: enhanced thermoelectric properties of Cu1–xZnxFeS2 with in situ nanoprecipitates. Advanced Energy Materials 2017, 7 (3), 1601299.
49. Yu H; Xu P; Lee D-W; Li X, Porous-layered stack of functionalized AuNP–rGO (gold nanoparticles–reduced graphene oxide) nanosheets as a sensing material for the micro-gravimetric detection of chemical vapor. Journal of Materials Chemistry A 2013, 1 (14), 4444–4450.
50. Hsieh Z-L; Lin M-C; Uan J-Y, Rapid direct growth of Li–Al layered double hydroxide (LDH) film on glass, silicon wafer and carbon cloth and characterization of LDH film on substrates. Journal of Materials Chemistry 2011, 21 (6), 1880–1889.
51. Kumar B; Singh SV; Chattopadhyay A; Biring S; Pal BN, Scalable Synthesis of a Sub-10 nm Chalcopyrite (CuFeS2) Nanocrystal by the Microwave-Assisted Synthesis Technique and Its Application in a Heavy-Metal-Free Broad-Band Photodetector. ACS omega 2020, 5 (40), 25947–25953. [PubMed: 33073121]
52. Gabka G; Bujak P; Żukrowski J; Zabost D; Kotwica K; Malinowska K; Ostrowski A; Wielgus I; Lisowski W; Sobczak JW, Non-injection synthesis of monodisperse Cu–Fe–S nanocrystals and their size dependent properties. Physical Chemistry Chemical Physics 2016, 18 (22), 15091–15101. [PubMed: 27197089]
53. Wang SS; Jiao L; Qian Y; Hu WC; Xu GY; Wang C; Jiang HL, Boosting Electrocatalytic Hydrogen Evolution over Metal–Organic Frameworks by Plasmon-Induced Hot-Electron Injection. Angewandte Chemie International Edition 2019, 58 (31), 10713–10717. [PubMed: 31155823]
54. Zheng Z; Tachikawa T; Majima T, Single-particle study of Pt-modified Au nanorods for plasmon-enhanced hydrogen generation in visible to near-infrared region. Journal of the American Chemical Society 2014, 136 (19), 6870–6873. [PubMed: 24779561]
55. Yang Q; Du J; Li J; Wu Y; Zhou Y; Yang Y; Yang D; He H, Thermodynamic and kinetic influence of oxygen vacancies on the solar water oxidation reaction of α-Fe2O3 photoanodes. ACS applied materials & interfaces 2020, 12 (10), 11625–11634. [PubMed: 32073812]
56. Li Y; Qian G; Brown PL; Gerson AR, Chalcopyrite dissolution: Scanning photoelectron microscopy examination of the evolution of sulfur species with and without added iron or pyrite. Geochimica et Cosmochimica Acta 2017, 212, 33–47.
57. Baffou G; Quidant R; García de Abajo FJ, Nanoscale control of optical heating in complex plasmonic systems. ACS nano 2010, 4 (2), 709–716. [PubMed: 20055439]
58. Nishikawa M; Nomoto K; Kume S; Nishihara H, Reversible copper (II)/(I) electrochemical potential switching driven by visible light-induced coordinated ring rotation. Journal of the American Chemical Society 2012, 134 (25), 10543–10553. [PubMed: 22630816]
59. Navon N; Golub G; Cohen H; Paoletti P; Valtancoli B; Bencini A; Meyerstein D, Design of ligands that stabilize Cu (I) and shift the reduction potential of the CuII/I couple cathodically in aqueous solutions. Inorganic chemistry 1999, 38 (15), 3484–3488. [PubMed: 11671093]
60. Kim TW; Choi K-S, Nanoporous BiVO4 photoanodes with dual-layer oxygen evolution catalysts for solar water splitting. Science 2014, 343 (6174), 990–994. [PubMed: 24526312]
61. Yin Q; Vaughan D; England K; Kelsall G; Brandon N, Surface oxidation of chalcopyrite (CuFeS2) in alkaline solutions. Journal of the Electrochemical Society 2000, 147 (8), 2945.
62. Grimaud A; Diaz-Morales O; Han B; Hong WT; Lee Y-L; Giordano L; Stoerzinger KA; Koper MT; Shao-Horn Y, Activating lattice oxygen redox reactions in metal oxides to catalyse oxygen evolution. Nature chemistry 2017, 9 (5), 457–465.
63. Amiri M; Fallahi M; Bezaatpour A; Jijie R; Nozari-Asbmarz M; Rouhi M; Boukherroub R; Szunerits S, Solution processable Cu (II) macrocycle for the formation of Cu2O thin film on indium tin oxide and its application for water oxidation. The Journal of Physical Chemistry C 2018, 122 (29), 16510–16518.
64. Drosou M; Kamatsos F; Ioannidis G; Zarkadoulas A; Mitsopoulou CA; Papatriantafyllopoulou C; Tzeli D, Reactivity and Mechanism of Photo-and Electrocatalytic Hydrogen Evolution by a Diimine Copper (I) Complex. Catalysts 2020, 10 (11), 1302.

65. Zhu D; Wang L; Yu W; Xie H, Intriguingly high thermal conductivity increment for CuO nanowires contained nanofluids with low viscosity. scientific reports 2018, 8 (1), 1–12. [PubMed: 29311619]

66. Liu H; Xie J; Liu P; Dai B, Effect of Cu+/Cu2+ ratio on the catalytic behavior of anhydrous nieuwland catalyst during dimerization of acetylene. Catalysts 2016, 6 (8), 120.

67. Shah PM; Burnett JW; Morgan DJ; Davies TE; Taylor SH, Ceria–zirconia mixed metal oxides prepared via mechanochemical grinding of carbonates for the total oxidation of propane and naphthalene. Catalysts 2019, 9 (5), 475.

68. Peng C-Y; Hou C-C; Chen Q-Q; Wang C-J; Lv X-J; Zhong J; Fu W-F; Che C-M; Chen Y, Cu (OH) 2 supported on Fe (OH) 3 as a synergistic and highly efficient system for the dehydrogenation of ammonia-borane. Science Bulletin 2018, 63 (23), 1583–1590.

69. Giester G; Libowitzky E, Crystal structures and Raman spectra of Cu (OH) F and Cu3 (OH) 2F4. Zeitschrift für Kristallographie-Crystalline Materials 2003, 218 (5), 351–356.

70. Deng Y; Handoko AD; Du Y; Xi S; Yeo BS, In situ Raman spectroscopy of copper and copper oxide surfaces during electrochemical oxygen evolution reaction: identification of CuIII oxides as catalytically active species. Acs Catalysis 2016, 6 (4), 2473–2481.

71. Jacintho GV; Corio P; Rubim JC, Surface-enhanced Raman spectra of magnetic nanoparticles adsorbed on a silver electrode. Journal of Electroanalytical Chemistry 2007, 603 (1), 27–34.

72. Li Z; Zhang L; Liu Y; Shao C; Gao Y; Fan F; Wang J; Li J; Yan J; Li R, Surface-Polarity-Induced Spatial Charge Separation Boosts Photocatalytic Overall Water Splitting on GaN Nanorod Arrays. Angewandte Chemie 2020, 132 (2), 945–952.

73. Furube A; Du L; Hara K; Katoh R; Tachiya M, Ultrafast plasmon-induced electron transfer from gold nanodots into TiO2 nanoparticles. Journal of the American Chemical Society 2007, 129 (48), 14852–14853. [PubMed: 17994750]

74. Du L; Xi W; Zhang J; Matsuzaki H; Furube A, Electron transfer dynamics and yield from gold nanoparticle to different semiconductors induced by plasmon band excitation. Chemical Physics Letters 2018, 701, 126–130.

75. Vigderman L; Zubarev ER, High-yield synthesis of gold nanorods with longitudinal SPR peak greater than 1200 nm using hydroquinone as a reducing agent. Chemistry of Materials 2013, 25 (8), 1450–1457.

76. Bolte S; Cordelières FP, A guided tour into subcellular colocalization analysis in light microscopy. Journal of microscopy 2006, 224 (3), 213–232. [PubMed: 17210054]

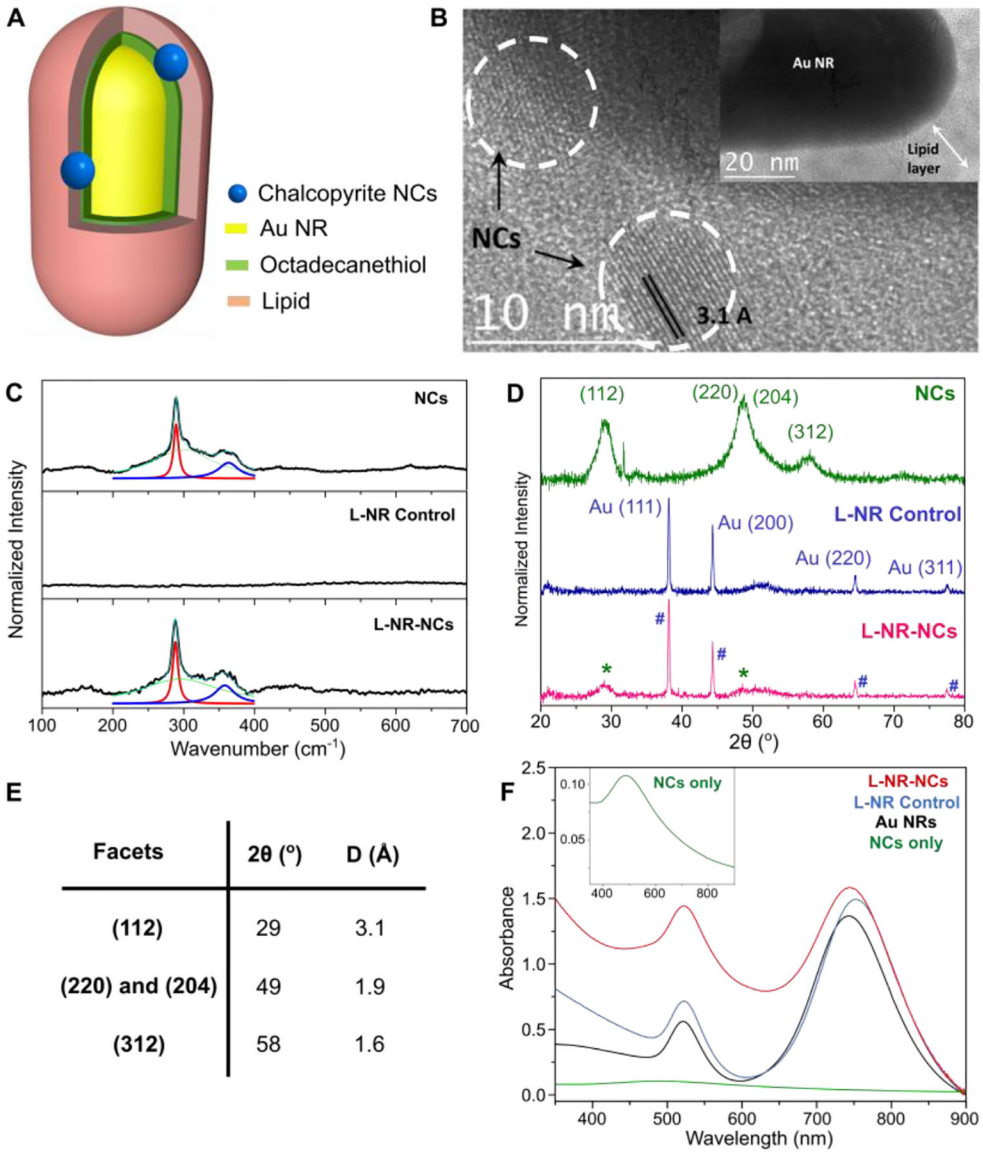

Facets	2θ (°)	D (Å)
(112)	29	3.1
(220) and (204)	49	1.9
(312)	58	1.6

Figure 1. Characterization of the Hybrid Plasmonic Photocatalyst.

(A, B) Structural scheme (A) and TEM micrographs (B) of the hybrid plasmonic photocatalyst (L-NR-NCs).

(C) Raman spectra of drop-casted thin films of chalcopyrite NCs (top), L-NR control (middle), and L-NR-NCs (bottom) with Lorentzian peak fittings of the A_1 (red) and B_2 (blue) phonon modes. Green: a fitted baseline curve; Cyan: sum of the fit curves.

(D) XRD spectra of NCs (top), L-NR control (middle) and L-NR-NCs (bottom). NCs and Au NRs diffraction peaks in L-NR-NCs are denoted respectively with asterisks (*) and pound (#) signs.

(E) Summary of the XRD diffraction angles (2θ) and interplanar distances (D) of different NCs facets.

(F) UV-vis absorbance spectra of L-NR-NCs (red), L-NR control (blue), Au NRs control not coated with hybrid membrane (black), and NCs only (green, inset); all controls contained the same Au and/or NCs concentrations as in L-NR-NCs (see Table S1 for concentrations).

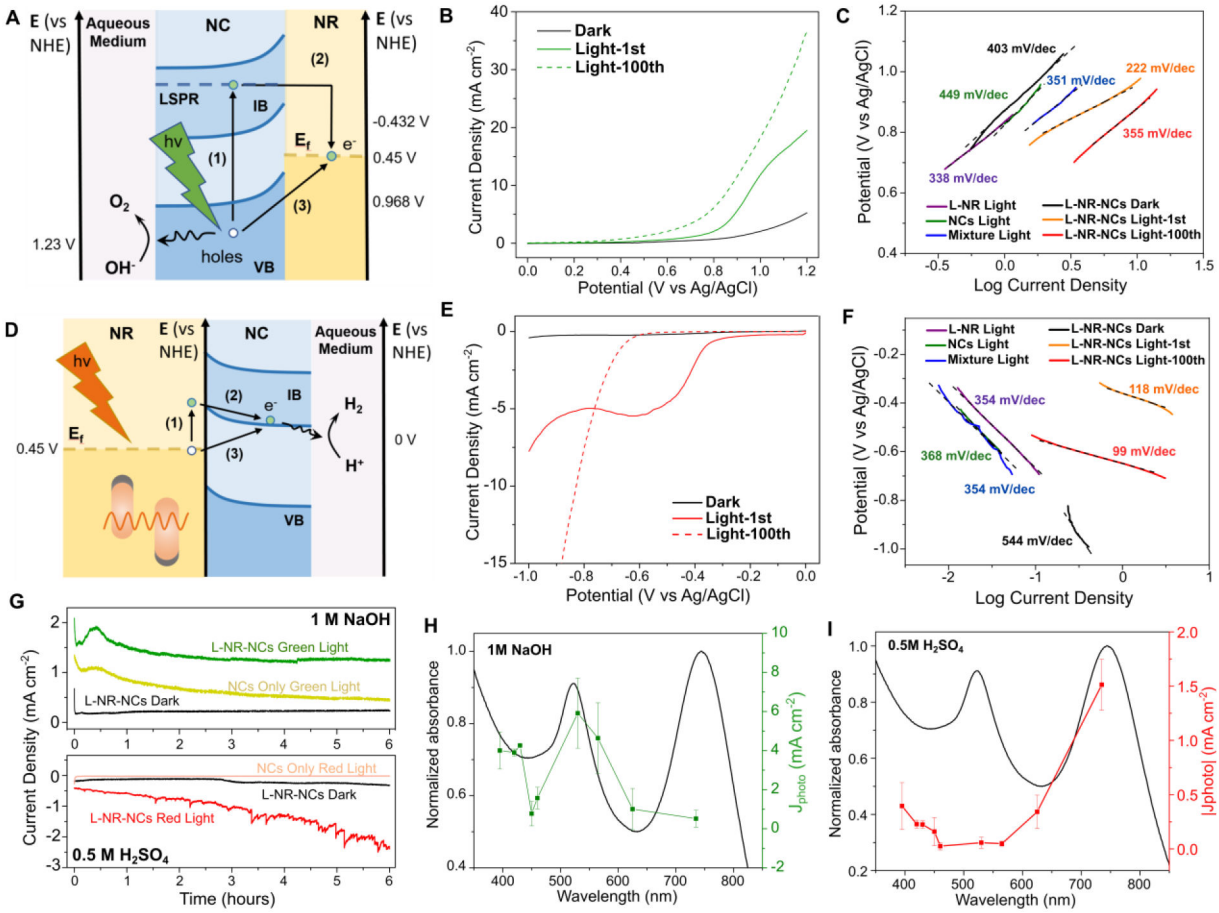

Figure 2. Photoelectrochemical Characterizations of the Hybrid Plasmonic Photocatalyst.

(A-C) Plasmonic charge transfer scheme (A), LSV curves (B), and Tafel Plot (C) for OER photocatalysis in 1 M NaOH by L-NR-NCs with green light irradiation from a 530 nm LED. Processes (1) and (2) describes an indirect hot charge carrier transfer pathway, whereas (3) describes a direct plasmonic charge carrier transfer in (A).

(D-F) Plasmonic charge transfer scheme (D), LSV curves (E), and Tafel plot (F) for HER photocatalysis in 0.5 M H_2SO_4 by L-NR-NCs with red light irradiation from a 730 nm LED. Processes (1) and (2) describes an indirect hot charge carrier transfer pathway, whereas (3) describes a direct plasmonic charge carrier transfer in (D).

(G) Chronoamperometry (CA) curves of L-NR-NCs or NCs only control in 1M NaOH with 0.8 V (*vs.* Ag/AgCl) applied bias (top), or in 0.5 M H_2SO_4 with −0.7 V applied bias (bottom), with or without light.

(H, I) Wavelength dependence of L-NR-NCs catalytic J_{photo} in 1 M NaOH at 0.8 V applied bias (H), or 0.5 M H_2SO_4 at −0.7 V applied bias (I). Black curves: absorbance spectra of L-NR-NCs water suspension; green/red curves: J_{photo} at different excitation wavelengths after 100 scans of activation. Error bars: Mean ± standard deviation of 3 independent measurements.

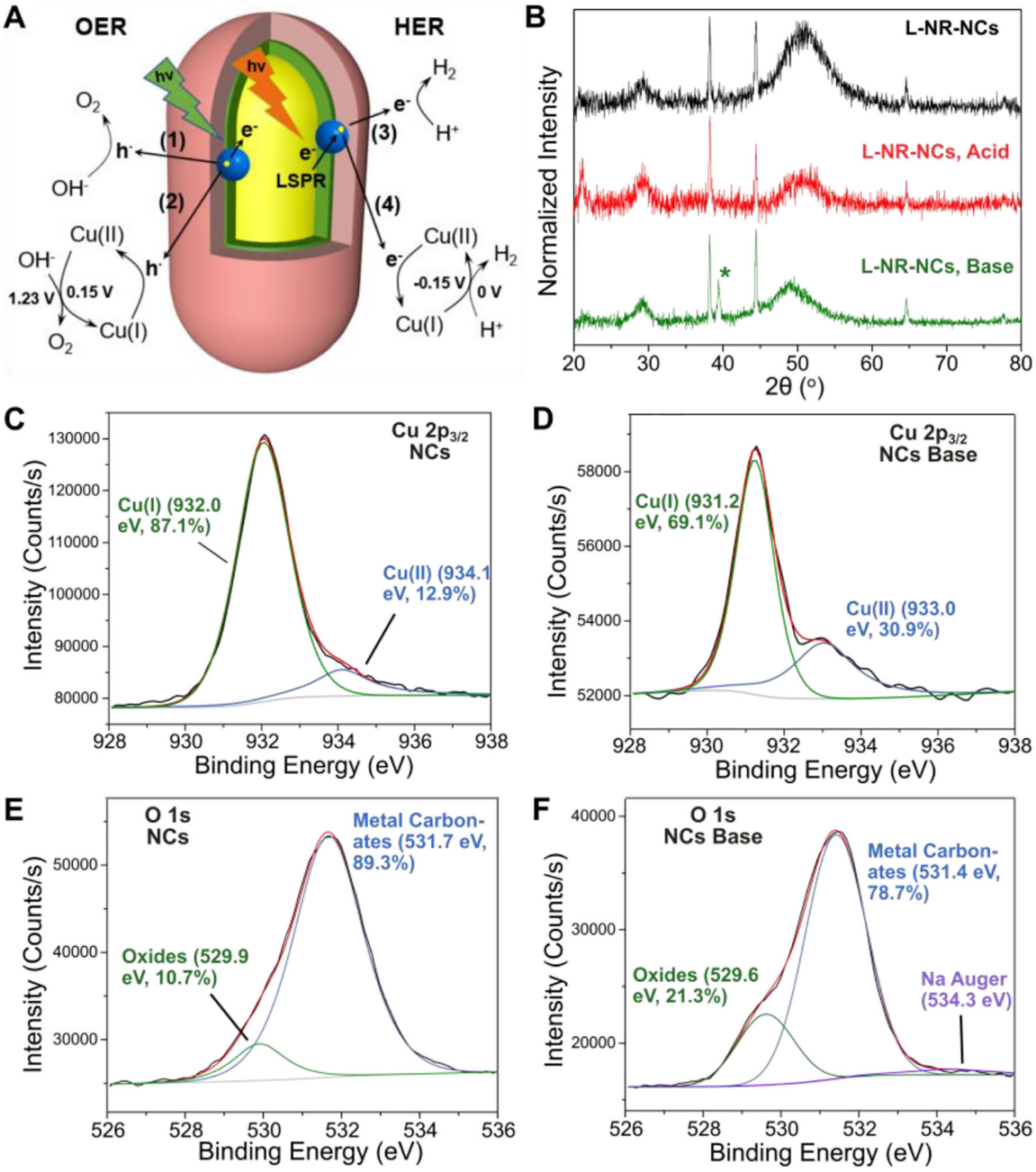

Figure 3. Characterization of the Composition and Oxidation States of the Hybrid Plasmonic Photocatalyst After PEC Measurements.

(A) Model of the charge transfer and redox processes for direct plasmonic charge carrier-induced photocatalysis ((1), (3)), and Cu(I)/Cu(II)-mediated catalysis ((2), (4)).

(B) XRD spectra of L-NR-NCs before any treatment (black), after cycling in 0.5 M H_2SO_4 with red light (red), and in 1 M NaOH with green light (green) for 1 hour. NC input concentrations are increased 10-fold in L-NR-NCs in this measurement compared to previous PEC measurements in order to magnify any compositional changes on the NCs.

(C, D) Cu $2p_{3/2}$ XPS spectrum (black) and fittings (red) with a Shirley baseline (light grey) for NCs before any treatment (C), and after cycling in 1 M NaOH with green light for 1 min (D).

(E, F) O 1s XPS spectrum (black) and fit (red) with a Shirley baseline (light grey) for NCs before any treatment (E), and after cycling in 1 M NaOH with green light for 1 min (F).

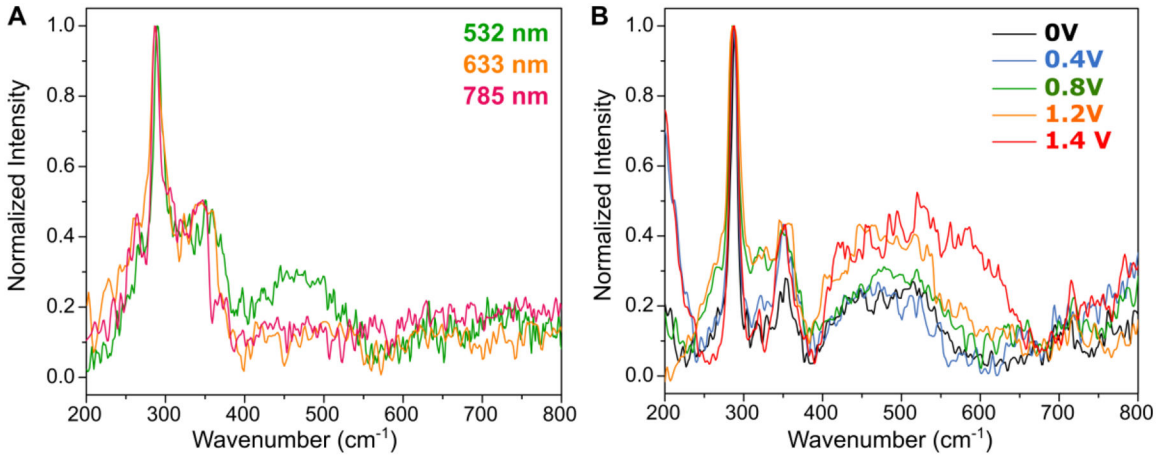

Figure 4. Raman Characterization of the OER Catalytic Mechanism of the Hybrid Plasmonic Photocatalyst.

(A) Raman spectra of L-NR-NCs drop-casted thin film at different excitation wavelengths of 532 nm (green), 633 nm (orange) and 785 nm (red).

(B) Raman spectra of L-NR-NCs drop-casted thin film on ITO substrate with different applied bias in the range of 0 – 1.4 V. All spectra were collected with 532 nm excitation.

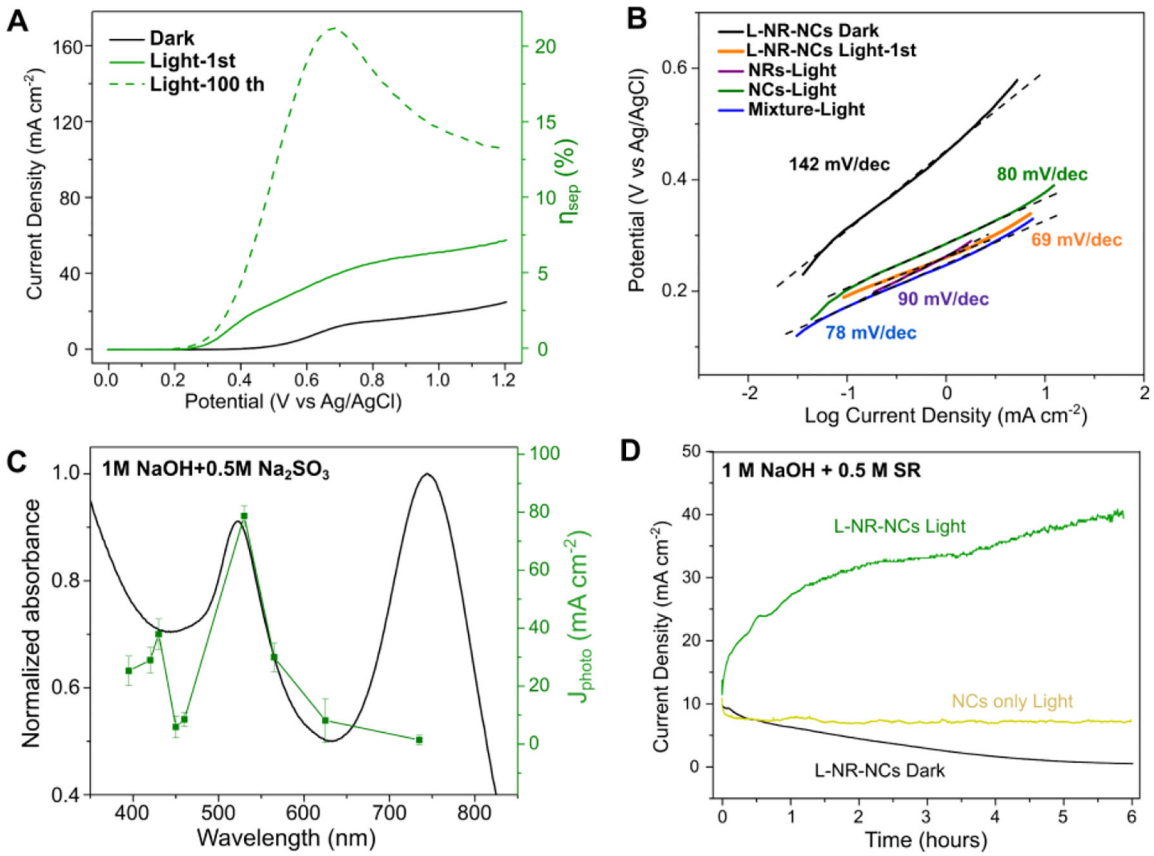

Figure 5. Study of the Mechanisms of the Plasmonic Photocatalyst with Sacrificial Reductant.

(A-B) LSV curves (A), and Tafel plot (B) of L-NR-NCs in 1 M NaOH + 0.5 M SR electrolyte with or without green light (530 nm LED) irradiation.

(C) Wavelength dependence of L-NR-NCs catalytic J_{photo} in 1 M NaOH + 0.5 M SR at 0.8 V applied bias in 1 M NaOH + 0.5 M SR electrolyte. Black curve: absorbance spectrum of L-NR-NCs water suspension. Green curve: J_{photo} at different excitation wavelengths after 100 scans of activation. Error bars: Mean ± standard deviation of 3 independent measurements.

(D) CA curves of L-NR-NCs or NCs only control in 1 M NaOH + 0.5 M SR electrolyte with 0.8 V (*vs.* Ag/AgCl) applied bias with or without green light (530 nm LED) irradiation.